Assessment of inhomogeneity in environmental conditions in a Norwegian fjord for design of floating bridges

Zhengshun Cheng[a,b,*], Erik Svangstu[c], Torgeir Moan[d], Zhen Gao[d]

[a] *State Key Laboratory of Ocean Engineering, Shanghai Jiao Tong University, Shanghai 200240, China*
[b] *SJTU Yazhou Bay Institute of Deepsea Science and Technology, Sanya 572024, China*
[c] *Norwegian Public Roads Administration, Leikanger, 6863, Norway*
[d] *Department of Marine Technology and Centre for Autonomous Marine Operations and Systems (AMOS), Norwegian University of Science and Technology (NTNU), Trondheim, 7491, Norway*

Abstract

Environmental conditions along a very large floating bridge are inhomogeneous due to complex topography and hydrography. Evaluating the inhomogeneity in environment conditions is important for safety design of floating bridges but challenging because of their large size. This study addresses the assessment of long-term spatial inhomogeneity in wind and wave parameters for environmental conditions in a Norwegian fjord for design of floating bridges based on 16-year hindcast data. The wind and wave data are numerically simulated by using the Weather Research and Forecasting (WRF) model and Simulating Waves Nearshore (SWAN) model, respectively. The accuracy of hindcast wave data is validated by comparison against field measurements. Inhomogeneity in wind and wave parameters are revealed by contour maps by considering two dominant wave directions. Significant wave height and peak period are fairly close in the south part and decrease gradually towards the north end. Mean wave direction decreases from south end to north end. Mean wind speed has a relatively small variation in the south part and a great variation in the north part, so do the mean wind direction. Correlation of wind and wave parameters along a potential bridge route is analyzed. Wind parameters are less correlated than the wave parameters.

Keywords: inhomogeneity, wind and wave, hindcast data, correlation, floating bridges

1. Introduction

A floating bridge is a very large floating structure (VLFS) constructed for the purpose of providing passage over wide and deep straits and fjords or over waters with very soft seabeds. In

*Corresponding author. State Key Laboratory of Ocean Engineering, Shanghai Jiao Tong University, Shanghai, China. Email address: zhengshun.cheng@sjtu.edu.cn

these waters, building a traditional bridge with fixed supports is usually very expensive, while a floating bridge is a promising alternative.

Floating bridges feature up to several kilometers long in size and are usually deployed in coastal regions. Compared to marine and offshore structures that are deployed in the open sea (e.g., offshore oil and gas platform, offshore wind turbines) and other VLFSs such as Mobile offshore base (MOB) and MegaFloats, floating bridges have a much larger size and are more flexible with a large number of eigenmodes (Cheng et al., 2018a). These eigenmodes can be excited by environmental loads, threatening the structural integrity and safety. Besides, since floating bridges are usually located in the coastal region with complex topography and hydrography, they suffer more complex environmental conditions. These environmental conditions can also vary along the very long bridge route, i.e. environmental conditions are inhomogeneous.

During the design of marine and offshore structures, environmental conditions are usually assumed to be homogeneous in short term to facilitate the design. A wave field is homogeneous when the wave spectra and directional spectra at each point are identical and the wave elevations among any two points are coherent, i.e., each frequency component of the wave elevation have a constant phase difference. Similarly, a wind field is homogeneous when the wind spectra and directional spectra at the same height are identical and wind speed among any two points in the space are coherent. For marine and offshore structures that are deployed in the open sea and with a relatively small size, the assumption of homogeneous environmental conditions is reasonable.

However, for floating bridges that are up to several kilometers long, such assumption might lead to great underestimation of structural responses and thus threaten the structural safety. Cheng et al. (2018b) investigated the inhomogeneous wave load effects on a 4600m long curved floating bridge and revealed that inhomogeneous wave conditions can cause much larger structural response, especially the weak axis bending moment, than the homogeneous wave conditions. Therefore, the inhomogeneity in environmental conditions should be properly evaluated for the structural safety design of very long floating bridges.

Environmental conditions and associated inhomogeneities in straits and fjords can be assessed by carrying out field measurements or numerical simulations. Field measurements of wave condition (e.g. by wave buoy (Cheng et al., 2019a)) and wind condition (e.g. by anemometer and LiDAR (Cheynet et al., 2017)) can usually provide local environmental conditions. For a several-km long floating bridge, field measurement of wind and wave conditions requires a large number of measurement devices in order to capture the inhomogeneity in the environmental conditions. Therefore, field measurements are not an economical approach to determine the inhomogeneity. Alternatively, numerical simulations are more promising.

To simulate environmental conditions in straits and fjords, macro-scale numerical simulations based on phase-averaged approaches are desirable from computational efficiency point of view. In

coastal regions, the SWAN (Simulating Waves Nearshore) model (Booij et al., 1999) is usually used to simulate the complex wave transformation caused by the bathymetry, wind and other factors. This model is based on phase-averaged energy balance equation and has been employed to simulate waves in the outer Rio de la Plata estuary (Dragani et al., 2008) and the Bjørnafjord (Lothe and Musch, 2015). With respect to the local wind conditions, it is usually modelled by the Weather Research and Forecasting (WRF) model (Skamarock et al., 2008), which is a numerical weather prediction (NWP) system designed to serve both atmospheric research and operational forecasting needs.

Based on macro-scale simulation results, mid-scale simulations can be conducted to model the wind and wave propagation in details. These simulations for waves usually use phase-resolved approaches, such as nonlinear potential flow based method (e.g. Engsig-Karup et al. (2012)), Navier-Stokes equation based method (e.g. Wang et al. (2017)). OceanWave3D (Engsig-Karup et al., 2012), developed by DTU, is a potential flow modeling tool which accounts for large-scale fully nonlinear and dispersive free surface wave modeling. It has been used to simulate wave propagation in coastal regions. Wang et al. (2017) carried out a large-scale CFD (computational fluid dynamics) modeling of wave propagation in Sulafjord for the Coastal Highway E39 project of Norway. Simulation results from SWAN were used as inputs to the CFD simulations. Besides, various model equations based on vertical averaging of the flow or/and perturbation analyses have also been applied to model wave propagation, such as, e.g. Boussinesq-type equations (Madsen et al., 2002) and Green–Naghdi equations (Green and Naghdi, 1976), and nonlinear variants of multimodal coupled mode equations. However, all these phase-resolved methods are usually more computational demanding than the phase-averaged methods. The wind and wave data used in the present study were thus simulated by using phase-averaged methods.

In the short-term description of wind and waves, normally wind in 10 minutes and waves in 3 hours are considered as stationary. When describing the combined wind and wave condition, a compromise is usually a duration of 1 hour for both wind and waves. Such compromise is also adopted in the present study.

In this study, the inhomogeneity in the environmental conditions (wind and waves) in a Norwegian fjord, i.e., the Bjørnafjord, is evaluated based on numerically simulated wind and wave data over about 16 years. The long-term joint distribution of wind and wave conditions in this fjord has been established by Cheng et al. (2019b) based on simulated data at one location in the fjord. The inhomogeneity in wind and wave conditions in this fjord is not studied yet, but it is of significant importance to the safety design of floating bridges. It should be noted that in general, the inhomogeneity of wind and wave conditions in a fjord consists of both long-term variation (e.g. distribution of significant wave height) of the wind and wave parameters in the fjord and the short-term variation (e.g. the wave spectra and the cross-spectra for the waves at different locations

in the fjord). In this paper, we only address the long-term spatial inhomogeneity of the wind and wave parameters, since the phase-averaged hindcast data were used.

2. Data description

The fjord considered in this study is the Bjørnafjord located at the Hordaland County, Norway. It is about 4600m wide and more than 500m deep. The location and topography of the fjord are shown in Fig. 1. The local bathymetry of the fjord is illustrated in Fig. 2. A floating bridge is planned to be built to cross the fjord by the Norwegian Public Roads Administration (NPRA). To achieve a safe, reliable and cost-effective design of floating bridge, the environmental condition in the fjord should be properly assessed.

Both numerical simulations and field measurements have been carried out to characterize the environmental condition in the fjord. These environmental data has been described in detail in Cheng et al. (2019a) and Cheng et al. (2019b). In this section, relevant environmental data is briefly described to better illustrate the results in this study.

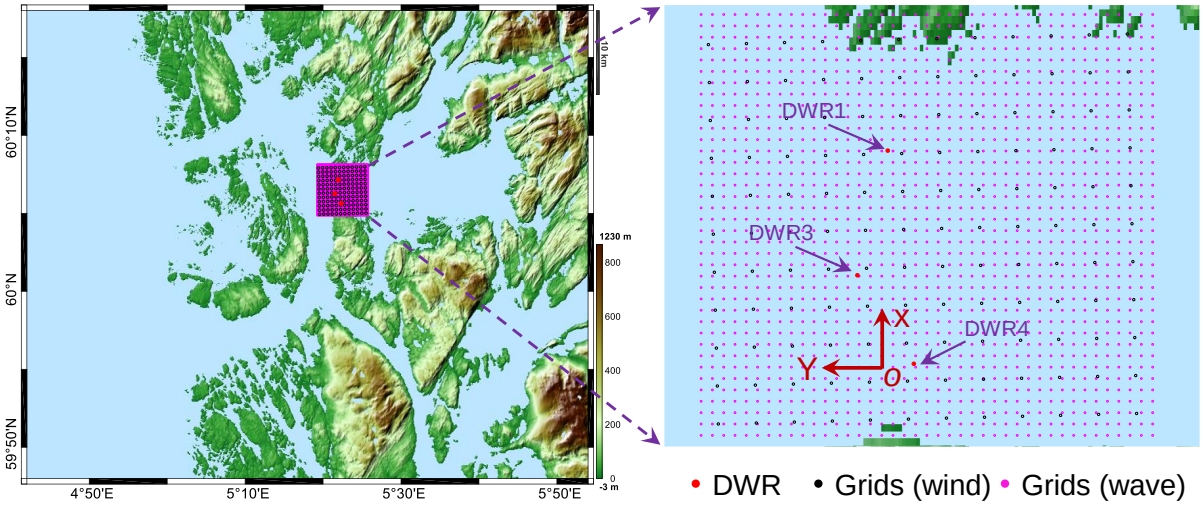

Figure 1: Location and topography of the Bjørnafjord. A close up view of the potential bridge site is shown in the right figure. Grid points for simulating wind and wave data and three Datawell waveriders (DWRs) are marked. A global coordinate system is defined, with the origin located at approximately 60°05′20.2″N and 5°21′55.7″E. X is positive towards north and Y is positive towards west.

2.1. Numerical simulations of wind and wave conditions

The wave condition in the fjord is simulated by using the SWAN (Simulating Waves Nearshore) model (Booij et al., 1999), a third-generation wave model. The model is a phase-averaged model

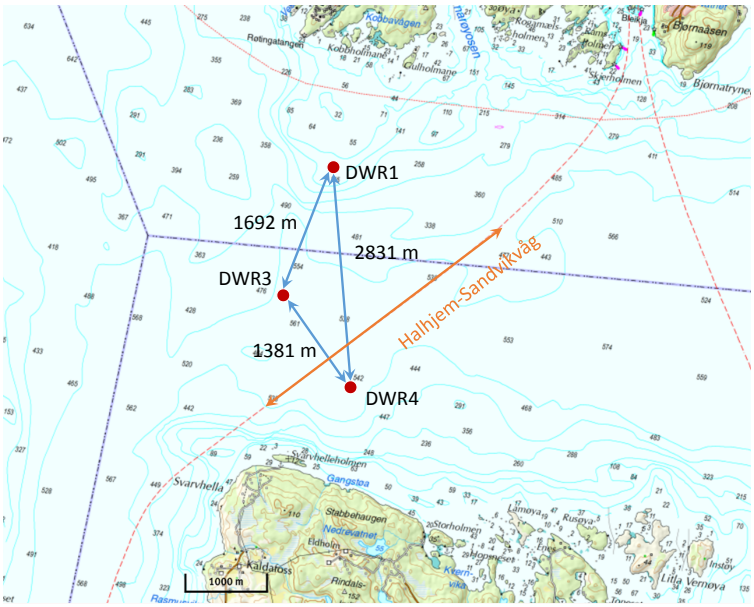

Figure 2: Local bathymetry of the Bjørnafjord (Cheng et al., 2019a). Location of the three Datawell waveriders (DWRs) are marked.

based on the wave action balance equation and solves the action density balance equation in time, geographical and spectral space. Therefore, it can provide wave-frequency spectrum and directional spectrum, and relevant wave parameters such as significant wave height, peak period and mean direction etc. The SWAN model has been widely used to simulate realistic estimates of wave parameters in coastal areas, lakes, estuaries from given wind, bottom and current conditions. It can simulate both wind-generated waves and swells. But in this study, only wind-generated waves are simulated for the fjord because the swell is very small (Cheng et al., 2019a). A total of 296×373 grid points, with a spacing of approximately 150m, are equally distributed in the area with latitude ranging from 59.85 to 60.2483 and longitude ranging from 4.8 to 5.797.

The wind condition in the fjord is simulated by using the WRF (Weather Research and Forecasting) model (Skamarock et al., 2008), a next-generation mesoscale numerical weather prediction system designed for both atmospheric research and operational forecasting applications. The model solves the compressible, nonhydrostatic Euler equations in time and geographical space and provides the mean wind speed at 10m height for each grid point in the latitude and longitude directions. In this study, a total of 138×180 with a spacing of about 500m are equally distributed for simulating mean wind speed.

A close up view of the grid points for simulating wind and wave conditions around the potential bridge site is shown in Fig. 1. Numerical simulation of wind and wave conditions are based on hindcast data from January 2002 to June 2017. Wind and wave parameters are stored in every hour,

including significant wave height, peak period, mean direction and mean wind speed in latitude and longitude directions.

2.2. Field measurements of wave conditions

Three Datawell waveriders (DWRs) were deployed to measure the wave conditions in the fjord by recording the heave, north and west displacements of the buoy. The measurements have been carried out since February 2016. Cheng et al. (2019a) analyzed the measured wave data from February 2016 to October 2017 and revealed that the waves in the fjord are short-crested and mainly wind-generated. Waves with a relatively large significant wave height ($H_s > 0.3$m) are likely to have one dominant direction, while small waves are likely to have multiple dominant directions.

In this study, a total of about 33 months (From February 2016 to October 2018) of measured raw data is used. The measured raw data are recorded and stored in 30 minutes samples with a frequency of 1.28 Hz. To make it consistent with simulated wave data, the measured raw data are post-processed to obtain wave data in every hour.

3. Validation of simulated data

The accuracy of simulated wave data is validated in the section by comparison against field measurements. The accuracy of simulated wave data at the location of DWR3 has been validated by Cheng et al. (2019b) by comparing the simulated significant wave height with the measured one. However, only one location point was considered by Cheng et al. (2019b). Since this study aims to investigate the inhomogeneity in environmental conditions in the fjord based on numerically simulated data, the accuracy of simulated environmental data at more location points are thus required to be validated in order to demonstrate the accuracy of representing the environmental fields by the simulated one.

In this study, numerically simulated wave data at three points, i.e., DWR1, DWR3 and DWR4, are compared against field measurements. The simulated data overlaps with the measured data for about 17 months, from February 2016 to June 2017. These overlapping data are used here. Fig. 3 shows the time series of simulated and measured significant wave height at the three DWRs from February 2016 to June 2017. It can be observed that these three DWRs were out of work during certain periods, due to out of power or collision with ships passing by etc. These missing data are not included in the present analyses. As a result, the effective data used cover a duration of 9932, 11917 and 11502 hours for the DWR1, DWR3 and DWR4, respectively.

A close-up view of time series of the simulated and measured significant wave height is presented in Fig. 4. It is found that at all three DWRs, the simulated significant wave height $H_{s,S}$ has

an overall good agreement with the measured significant wave height $H_{s,M}$. A small discrepancy between $H_{s,S}$ and $H_{s,M}$ also exists. The discrepancy and accuracy are thus further quantified by statistical analyses and distribution analyses in the following sections.

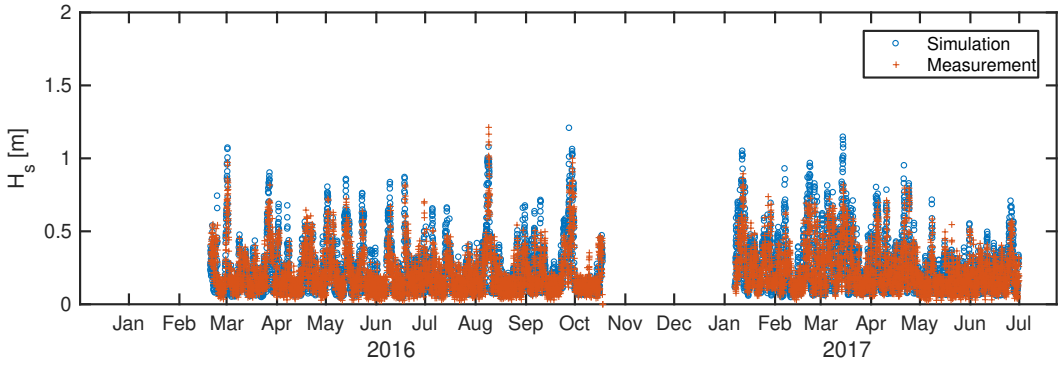

(a) DWR1

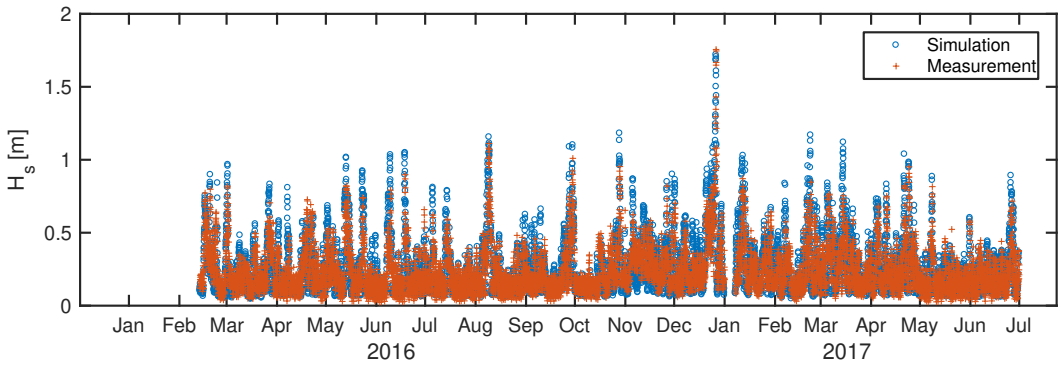

(b) DWR3

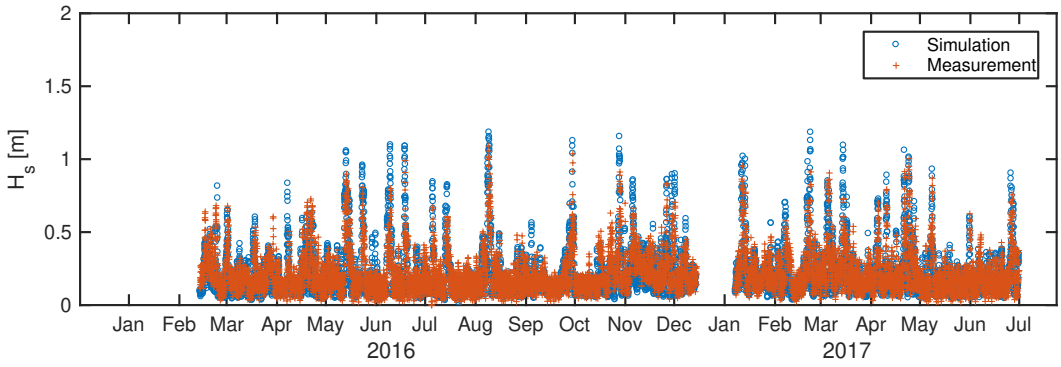

(c) DWR4

Figure 3: Comparison of time series of measured and simulated significant wave height at (a) DWR1, (b) DWR3, (c) DWR4 from February 2016 to June 2017.

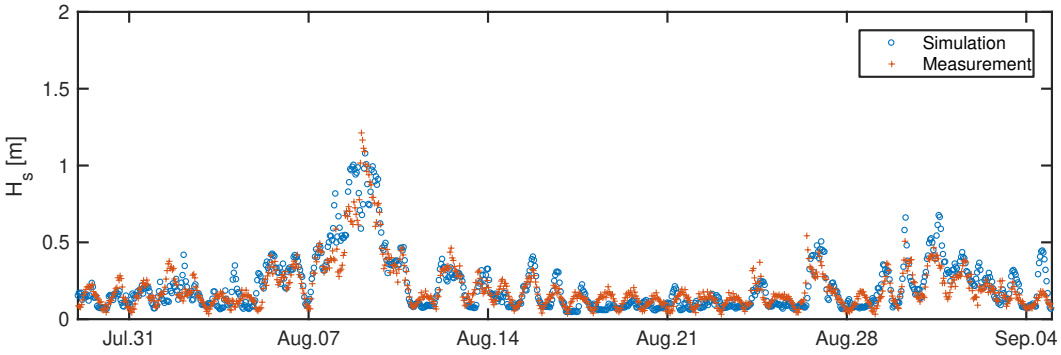

(a) DWR1

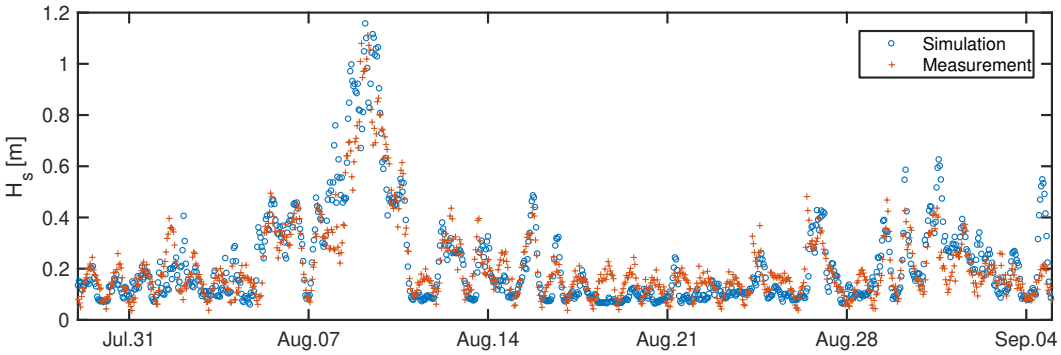

(b) DWR3

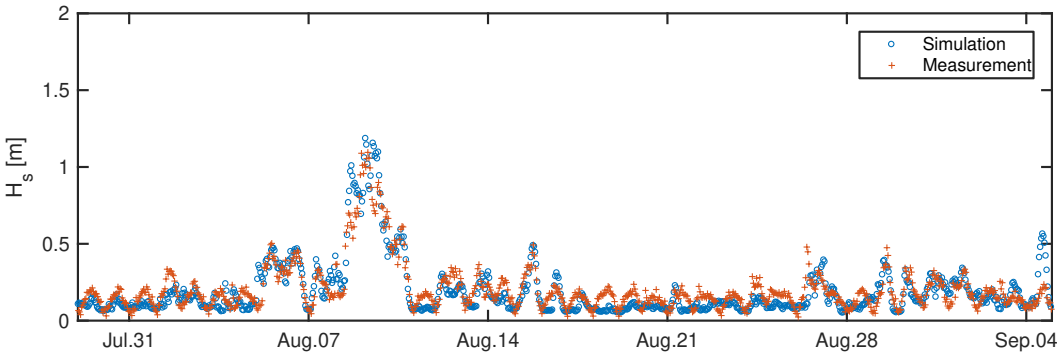

(c) DWR4

Figure 4: Comparison of time series of measured and simulated significant wave height at (a) DWR1, (b) DWR3, (c) DWR4 during August 2016.

3.1. Statistical analyses

A scatter plot of the simulated and measured significant wave height is shown in Fig. 5. To quantify the discrepancy, three statistical parameters are introduced here, including the bias, the root mean square error (RMSE) and the model uncertainty. The bias denotes the correspondence between the mean values of measured and simulated significant wave height. The RMSE provides

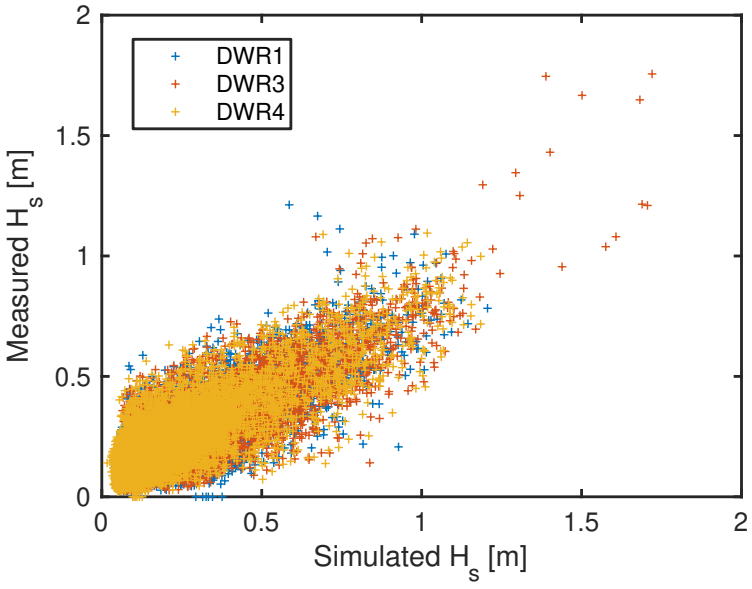

Figure 5: Scatter plot of simulated and measured significant wave height, ΔH_s, from February 2016 to June 2017 at the three DWRs.

a quantitative measure of the difference between time series data points of simulated and measured significant wave heights. The bias and RMSE are defined as follows

$$RMSE = \sqrt{\frac{1}{N}\sum_{j=1}^{N}\left(H_{s,S_j} - H_{s,M_j}\right)^2} \tag{1}$$

$$Bias = \frac{1}{N}\sum_{j=1}^{N}\left(H_{s,S_j} - H_{s,M_j}\right) \tag{2}$$

where N represents the total data point number of measured and simulated H_s. H_{s,S_j} and H_{s,M_j} denote the j^{th} data point in the time series of simulated and measured significant wave height, respectively.

The calculated bias and RMSE between the simulated and measured significant wave height at the three DWRs are given in Table 1. The bias at the three DWRs are all very small, close to zero, implying that the mean values between the time series of simulated and measured significant wave height are very close. The RMSE at the three DWRs are all approximately 0.1. This indicates the overall good consistency in accuracy with respect to simulated significant wave height at the three DWRs.

Model uncertainty is also studied here to represent the modeling uncertainties in the numerically simulated data. The model uncertainty is defined as the ratio of measured H_s to simulated

Table 1: Bias and root mean square error (RMSE) between simulated and measured significant wave height at the three DWRs.

	DWR1	DWR3	DWR4
Bias	0.006	0.007	-0.019
RMSE	0.098	0.105	0.098

H_s, given by

$$X = \frac{H_{s,M_j}}{H_{s,S_j}} \tag{3}$$

For each data point in the time series, a value of X can be estimated. Accordingly, the coefficient of variation (CoV) of model uncertainty X, defined as the ratio of the standard deviation σ_X to the mean μ_X, can be estimated by

$$CoV_X = \frac{\sigma_X}{\mu_X} \tag{4}$$

The mean value and coefficient of variation (CoV) of model uncertainty X are given in Table 2. Since the waves in this study are fairly small, several thresholds are thus introduced together with model uncertainty, in order to characterize the model uncertainty at different levels. It is found that given a threshold significant wave height $H_{s,thr}$, not only the mean value but also CoV of the model uncertainty X are generally close for the simulated significant wave height at the three DWRs. For a threshold significant wave height $H_{s,thr}$ larger than 0.6m, the mean value of model uncertainty X are about 0.784, 0.767 and 0.775 for the simulated significant wave height at DWR1, DWR3 and DWR4, respectively, and the corresponding CoV of X are respectively about 0.228, 0.228 and 0.241. Furthermore, as the threshold increases, both the mean value and CoV of the model uncertainty X decrease. This implies that at a higher threshold level, the prediction of simulated significant wave height presents a smaller variability.

Table 2: Mean value and coefficient of variation (CoV) of model uncertainty of simulated significant wave height H_S at DWR1, DWR3 and DWR4. Here $H_{s,thr}$ is the threshold of simulated H_s. The model uncertainty is calculated when simulated $H_{s,S}$ is larger than $H_{s,thr}$.

$H_{s,thr}$	Model uncertainty					
	Mean			CoV		
	DWR1	DWR3	DWR4	DWR1	DWR3	DWR4
0	1.164	1.171	1.351	0.502	0.497	0.526
0.3	0.832	0.821	0.864	0.307	0.289	0.305
0.6	0.784	0.767	0.775	0.228	0.228	0.241
1	0.749	0.778	0.759	0.153	0.191	0.177

3.2. *Distribution analyses*

The marginal distribution of the simulated and measured significant wave height are analyzed and compared in this section. Fig. 6 shows the Weibull plot of marginal distribution of simulated and measured significant wave height at the three DWRs from February 2016 to June 2017. Similar to Cheng et al. (2019b), it is found here that the simulated significant wave height follows a Weibull distribution, especially for the upper tail region; while the measured significant wave height can be described by a hybrid lognormal and Weibull distribution, i.e., the Lonowe model developed by Haver (1980).

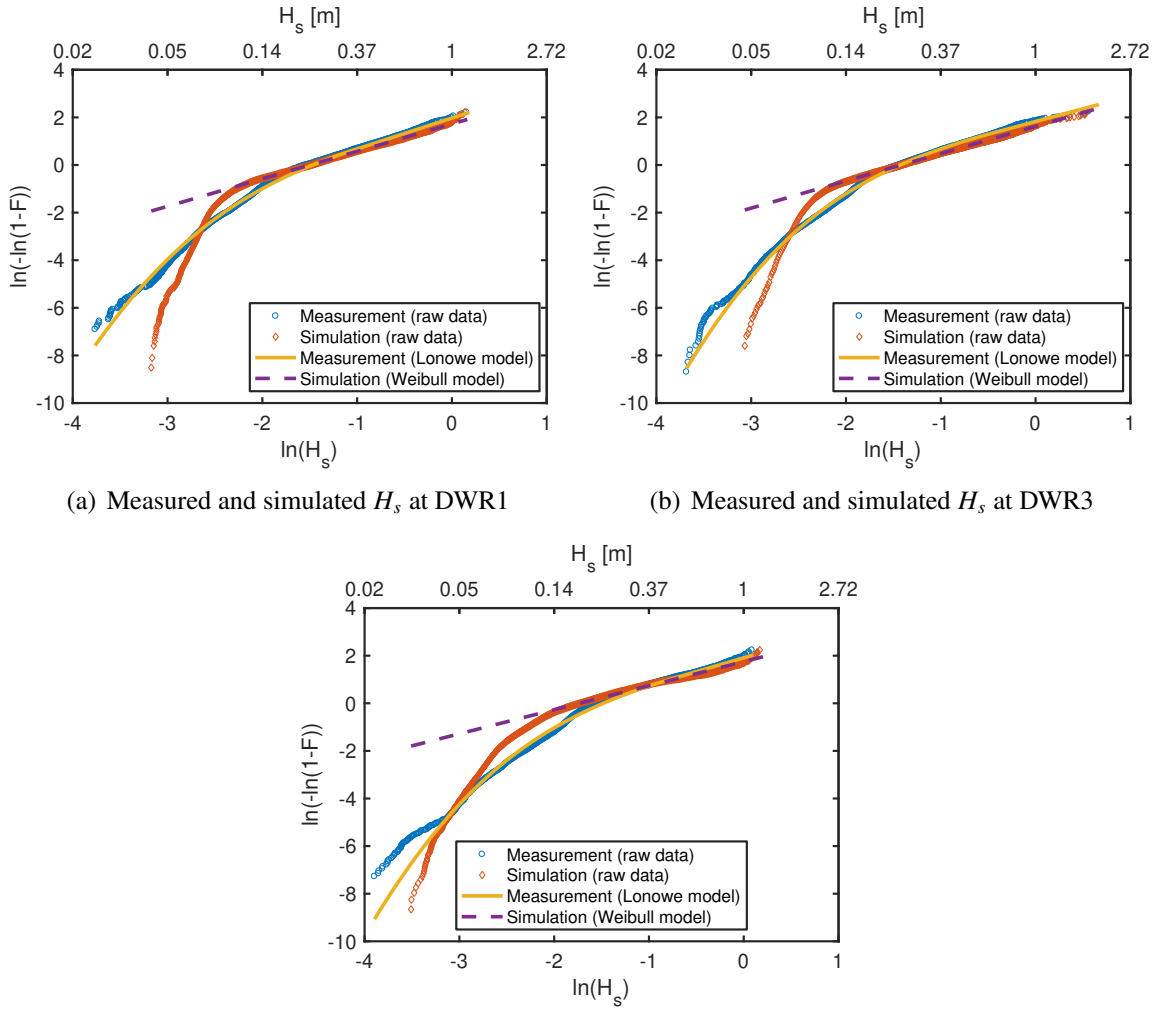

(a) Measured and simulated H_s at DWR1

(b) Measured and simulated H_s at DWR3

(c) Measured and simulated H_s at DWR4

Figure 6: Weibull plot of marginal distribution of simulated and measured significant wave height H_s from February 2016 to June 2017. (a) measured and simulated H_s at DWR1, (b) measured and simulated H_s at DWR3, (c) measured and simulated H_s at DWR4.

From practical design point of view, relatively large significant wave height is important. It

is therefore suitable to fit the raw data of the simulated significant wave height with H_s larger than 0.1m by a Weibull distribution. The probability density function (PDF) of a two-parameter Weibull distribution is given by

$$f_{H_{s,S}}(h) = \frac{\alpha}{\beta}\left(\frac{h}{\beta}\right)^{\alpha-1} \exp\left[-\left(\frac{h}{\beta}\right)^{\alpha}\right] \tag{5}$$

where α and β denote the shape and scale parameters, respectively.

For the measured significant wave height, the raw data in the upper tail follow a Weibull distribution, while the lower tail part follows a log-normal distribution. The Lonowe model is thus employed to describe the marginal distribution of measured H_s. The PDF of the Lonowe model is written as

$$f_{H_{s,M}}(h) = \begin{cases} \frac{1}{\sqrt{2\pi}\sigma h} \cdot \exp\left[-\frac{1}{2}\left(\frac{\ln(h)-\mu}{\sigma}\right)^2\right] & \text{if } h \le h_0 \\ \frac{\alpha}{\beta}\left(\frac{h}{\beta}\right)^{\alpha-1} \exp\left[-\left(\frac{h}{\beta}\right)^{\alpha}\right] & \text{if } h > h_0 \end{cases} \tag{6}$$

where h_0 is the shifting point from the lognormal distribution to the Weibull distribution, μ and σ are the mean value and standard deviation of $\ln(H_s)$ in the lognormal distribution. α and β are the shape and scale parameters in the Weibull distribution. The method for estimating the parameters in the Lonowe model is described by Haver (1980) and Moan et al. (2005) and is not explained in detail here. The basic idea is to estimate the Weibull parameters α and β by imposing the continuity condition of cumulative distribution function (CDF) and PDF at the shifting point.

The parameters involved in the distributions are estimated by fitting the hourly sampled raw data with analytical distributions. The fitted distributions for the simulated and measured significant wave height at the three DWRs are also plotted in Fig. 6. The Weibull parameters and extreme significant wave height estimated from raw data and fitted distribution are collected, as given in Table 3.

Table 3: Comparison of Weibull parameters and significant wave height H_s estimated from measured and simulated wave data based on raw data and fitted distribution. Data from February 2016 to June 2017 is considered here.

Data		DWR1		DWR3		DWR4	
		Measurement	Simulation	Measurement	Simulation	Measurement	Simulation
Weibull parameters	α	1.298	1.154	1.071	1.145	1.168	1.011
	β	0.219	0.224	0.182	0.242	0.195	0.177
Raw data	1-year H_s	1.156	1.141	1.711	1.699	1.077	1.173
Fitted Distribution	1-year H_s	1.196	1.516	1.425	1.664	1.288	1.571
	10-year H_s	1.424	1.844	1.760	2.027	1.563	1.965
	100-year H_s	1.641	2.164	2.090	2.381	1.830	2.358

The 1-year H_s estimated from the raw data is very close between the measured and simulated data. However, the 1-year H_s estimated from the fitted distribution differs between the measured and simulated data. This is because for all the three DWRs, the fitted Weibull parameters (both α and β) based on the measured data differ from those based on the simulated data. Moreover, Table 3 presents significant difference in 10-year and 100-year H_s estimated from fitted distributions based on the measured and simulated data. These differences are due to model uncertainties. These 100-year H_s are estimated based on about 14 months raw data, which of course cause large uncertainty in the predicted 100-year value. Based on statistical analysis of 37-year hindcast data, Moan et al. (2005) revealed that the 100-year H_s predicted based on 1-year raw data exhibits great uncertainty, with a ratio of the maximum predicted 100-year H_s to the minimum predicted 100-year H_s about 2. For the present study, the ratio of the predicted 100-year H_s based on the simulated and measured raw data is 1.32, 1.14 and 1.29 for DWR1, DWR3 and DWR4, respectively. Besides, the relative change of the predicted 100-year H_s is also of interest and defined as $\left(H_{s,100,sim} - H_{s,100,mea}\right)/H_{s,100,mea} \times 100\%$. The relative change of the predicted 100-year H_s are 31.9%, 13.9% and 28.9% for DWR1, DWR3 and DWR4, respectively. Therefore, the discrepancy in the predicted 100-year H_s between the measured and simulated data is still in a reasonable range.

4. Inhomogeneity of environmental conditions for design of floating bridges

In this section, the inhomogeneity of environmental conditions in the fjord is assessed from a statistical point of view. The potential area for deploying the floating bridges is highlighted in Fig. 7, i.e., within the purple dash lines. Environmental conditions in this area is of great interest. The wind and wave conditions in this area are thus analyzed in detail.

There are a total of 29×7 grid points (29 points along the global X direction and 7 points along the global Y direction) in the potential area. These grid points are originally used in the SWAN model. Wave parameters at these grid points, including significant wave height, peak period and mean direction, are thus already available from the hindcast data. Regarding the wind parameters (mean wind speed and direction) at these grid points, they are estimated by linear interpolation of available wind parameters in neighboring grid points, as shown in Fig. 1.

To characterize the inhomogeneity, the environmental parameters at each grid point are normalized by the corresponding environmental parameters at the reference point. In this study, the location at DWR3 is chosen as the reference point, since it is located in the middle of the fjord and the long-term joint distribution of parameters for wind and wave conditions has been established based on hindcast data at DWR3 (Cheng et al., 2019b). Relevant environmental parameters are

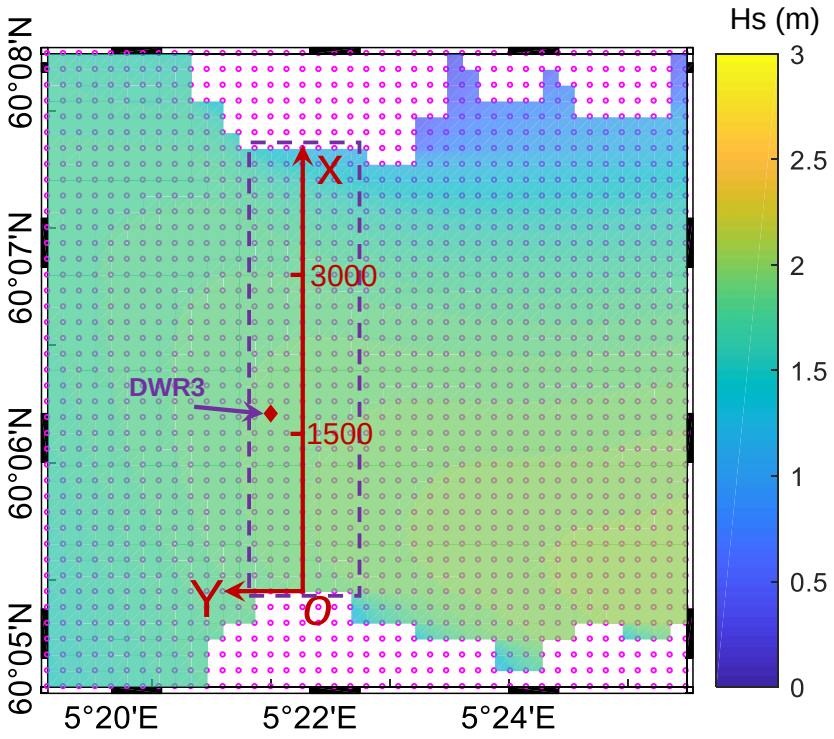

Figure 7: Illustration of analyzing points for wind and wave data. Pink points indicate the grid points for wave simulation. Grid points within the purple dash lines are assumed to be within the potential area for deploying a floating bridge and are considered for further analyses.

normalized as follows

$$\hat{H}_s = \frac{H_s}{H_{s,ref}} \tag{7}$$

$$\hat{T}_p = \frac{T_p}{T_{p,ref}} \tag{8}$$

$$\hat{U}_w = \frac{U_w}{U_{w,ref}} \tag{9}$$

$$\hat{\theta}_{wa} = \theta_{wa} - \theta_{wa,ref} \tag{10}$$

$$\hat{\theta}_{wi} = \theta_{wi} - \theta_{wi,ref} \tag{11}$$

Based on the field measured wave data, Cheng et al. (2019a) revealed that the waves in the fjord are mainly wind-generated and are mainly from east and northwest. Waves from southwest are also observed in the measured wave data, but they are less frequent than those from east and northwest.

250 However, the dominant wave directions based on hindcast data differ slightly from those based on the measured data. The long-term probability distribution of wind and wave directions at DWR3 is shown in Fig. 8 based on hindcast wind and wave data from 2002-2017. It can be found that not only waves from east and northwest, but also from southwest are observed. The discrepancy in terms of waves from southwest between numerical simulations and field measurements may be
255 due to the difference in hindcast wind directions. To make it consistent with the measured wave data, only waves from east and northwest are considered and analyzed in this study.

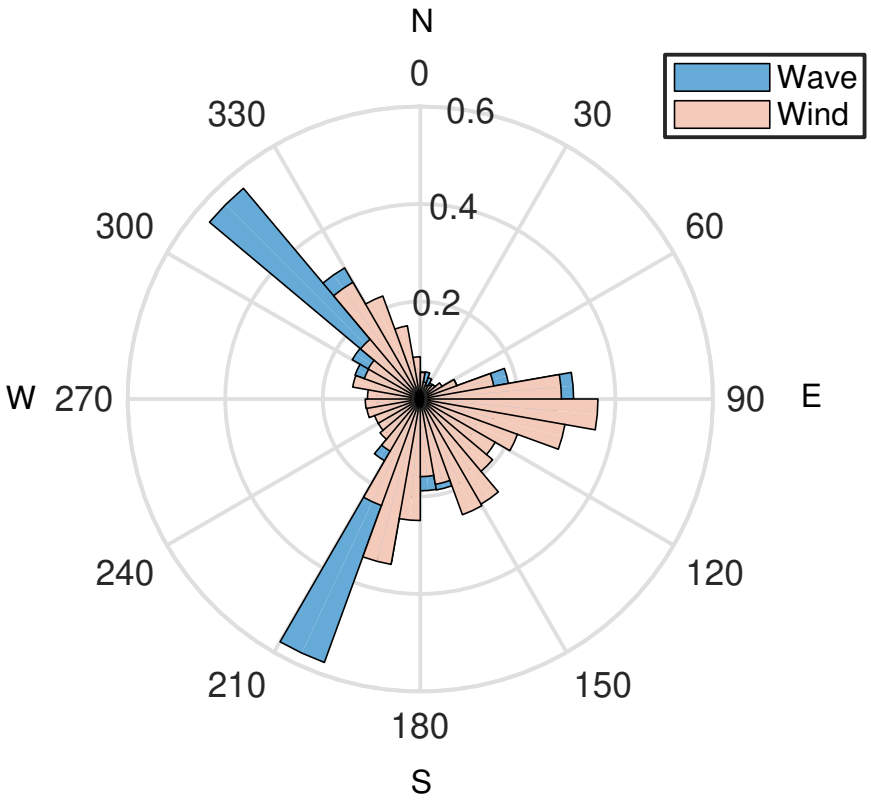

Figure 8: Long-term probability distribution of wind and wave directions at DWR3 based on simulated data from 2002 to 2017.

Cheng et al. (2019a) also revealed that waves with a relatively small significant wave height (less than 0.3m) are likely to have multiple dominant directions, while waves with a relatively large significant wave height are likely to have one dominant direction. In the numerical simula-
260 tions, these multiple dominant directions are not captured. Therefore, this study only considers the inhomogeneity in environmental conditions that consists of waves with a relatively large significant wave height. These environmental conditions are also the design-driven conditions in the design of floating bridges. A threshold significant wave height, denoted by $H_{s,thr}$, is thus introduced here. It is defined with respect to the significant wave height at the reference point $H_{s,ref}$.

The inhomogeneity is estimated when $H_{s,ref}$ is larger than or equal to $H_{s,thr}$.

In this section, the variation of environmental parameters across the fjord is addressed by considering two dominant wave directions, from northwest and from east. The variation of wind and wave parameters is demonstrated by using the contour map, in which the same contour line represents the same value of the long-term statistical parameter (i.e. mean value or standard deviation in this study) for the normalized wind and wave parameters considered. Inhomogeneity in environmental parameters with waves from northwest is studied first.

4.1. Inhomogeneity in environmental parameters with waves from northwest

Figs. 9- 13 present the contour maps of mean values and standard deviations of normalized environmental parameters across the fjord. The mean values and standard deviations are estimated based on environmental conditions with waves from northwest and with a significant wave height at the reference point larger than a threshold value. Two representative threshold values of significant wave height, i.e., 0.3m and 0.6m, are considered in this section. The threshold value of significant wave height of 0.3m is selected based on previous studies (Cheng et al., 2019a,b) and was determined as a compromise between avoiding uncertain low sea states, having sufficient data for statistical analysis and focusing on waves of interest for practical design of floating bridges.

The variation of significant wave height across the fjord under two different threshold significant wave heights is demonstrated in Fig. 9. In general, the contour maps of mean values and standard deviations of normalized significant wave height $\hat{H}_s$ between the two different threshold significant wave heights are fairly similar. The mean values of $\hat{H}_s$ increase gradually from about 0.5 at north (X=4000m) to about 1 at south (X=0m) in the considered area. A rapid increase in the mean value of $\hat{H}_s$ mainly occurs in the north part of the considered area, with X ranging from about 4000m to about 3000m. This is because waves from northwest are accounted for here and the north side of the fjord provides certain shield effects to reduce the wave height. Regarding the standard deviation of $\hat{H}_s$, the largest standard deviation, approximately 0.14, is observed in the north end (X>4000m) of the considered area, while the smallest standard deviation, about 0.02, is located in the south part (1000m<X<2000m).

The variation of peak period across the fjord under two different threshold significant wave heights is shown in Fig. 10. Under the two different threshold significant wave heights, contour maps of mean values and standard deviations of normalized peak period $\hat{T}_p$ are very similar. The mean value of $\hat{T}_p$ has very small variation. For X ranges from 0m to 3000m, the mean value of $\hat{T}_p$ is close to 1. When X increases from 3000m to the north end, the mean value decreases gradually and reaches about 0.9 at the north end. The standard deviation of $\hat{T}_p$ is very small, close to 0. Slightly large standard deviations are observed in the north part of the considered area. In general, $\hat{T}_p$ has fairly small variations across the fjord. This also agrees with the finding by Cheng et al.

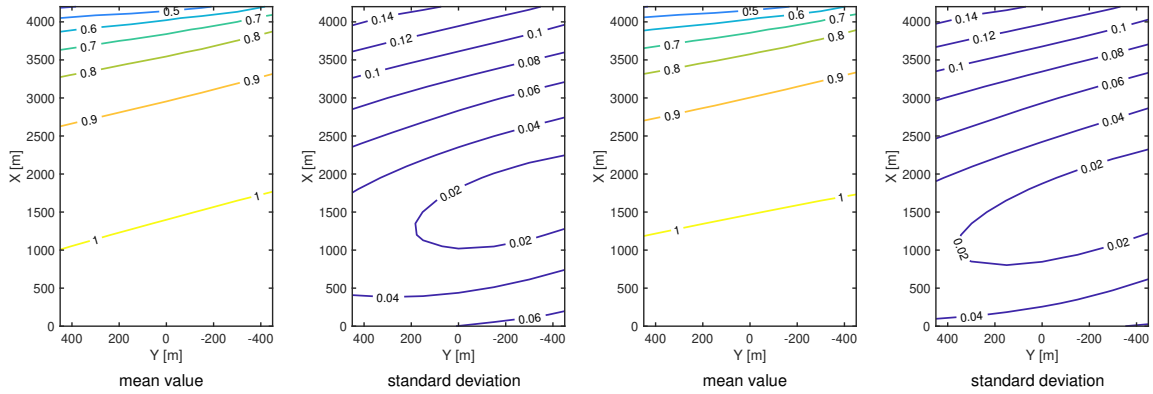

(a) $H_{s,thr}$ = 0.3m (b) $H_{s,thr}$ = 0.6m

Figure 9: contour maps of mean values and standard deviations of normalized significant wave height $\hat{H}_s$ across the fjord. Only environmental conditions with waves from northwest and with a significant wave height at the reference point larger than the threshold value $H_{s,thr}$ are considered here.

(2019a) based on analyzing field measured data by the three wave buoys.

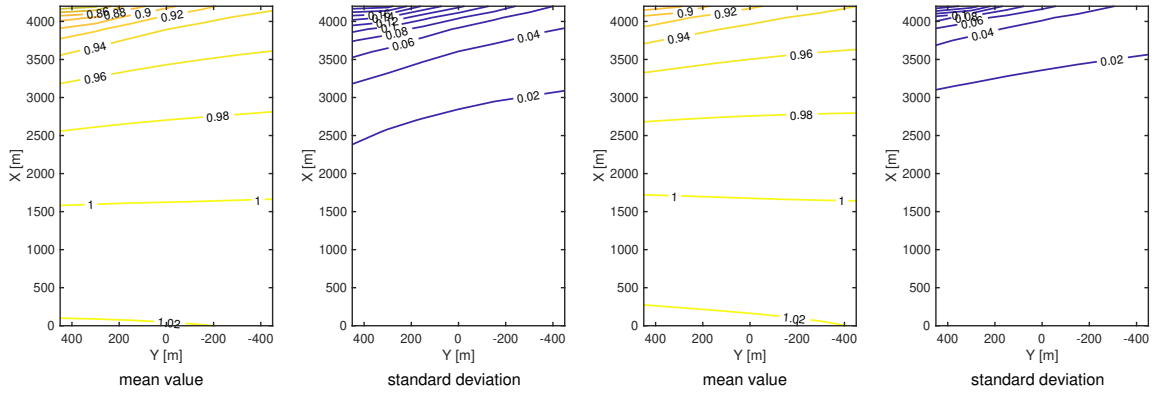

(a) $H_{s,thr}$ = 0.3m (b) $H_{s,thr}$ = 0.6m

Figure 10: contour maps of mean values and standard deviations of normalized peak period $\hat{T}_p$ across the fjord. Only environmental conditions with waves from northwest and with a significant wave height at the reference point larger than the threshold value $H_{s,thr}$ are considered here.

Fig. 11 shows the inhomogeneity in terms of normalized wave direction $\hat{\theta}_{wa}$ across the fjord. Here waves come from northwest and two threshold values of significant wave heights are considered. $\hat{\theta}_{wa}$ varies with a certain pattern across the fjord. The mean value of $\hat{\theta}_{wa}$ increases gradually from north to south, and the variation is approximately 30 degrees. The standard deviation of $\hat{\theta}_{wa}$ in the south part of the fjord (0m<X<3000m) is relatively small, less than 2 degrees. However, the standard deviation of $\hat{\theta}_{wa}$ in the north part of the fjord is relative larger than those in the south part. The standard deviation of $\hat{\theta}_{wa}$ can reach more than 12 degrees, especially under cases with a

threshold significant wave height of 0.3m. In addition, the mean value and standard deviation of $\hat{\theta}_{wa}$ between threshold values of significant wave heights of 0.3m and 0.6m are fairly similar.

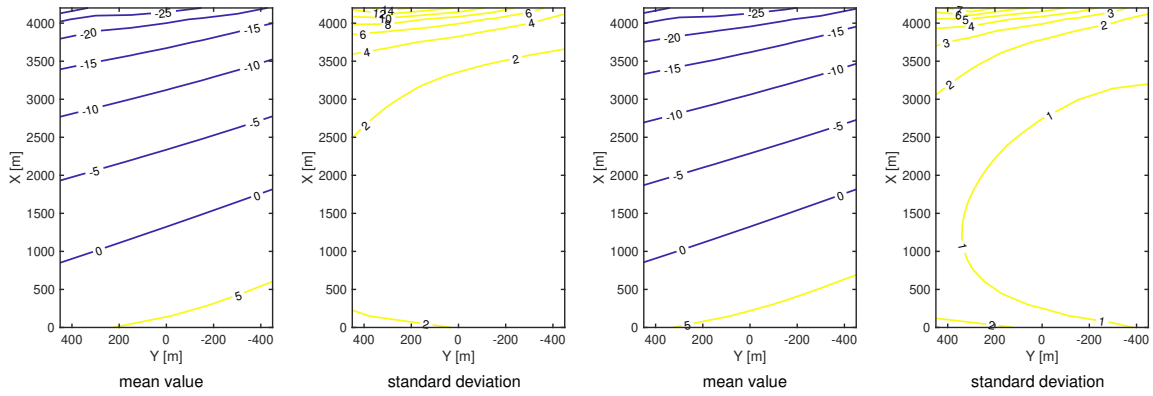

(a) $H_{s,thr}$ = 0.3m (b) $H_{s,thr}$ = 0.6m

Figure 11: contour maps of mean values and standard deviations of normalized wave direction $\hat{\theta}_{wa}$ across the fjord. Only environmental conditions with waves from northwest and with a significant wave height at the reference point larger than the threshold value $H_{s,thr}$ are considered here.

The mean wind speed has relatively larger variations across the fjord compared to the significant wave height and peak period. The contour maps of mean values and standard deviations of normalized mean wind speed $\hat{U}_w$ across the fjord under two different threshold significant wave heights is shown in Fig. 12. Different from $\hat{H}_s$ and $\hat{T}_p$, mean values of $\hat{U}_w$ that are slightly larger than 1 are observed in the central part of the considered area (1000m<X<3000m). In addition, the standard deviations of $\hat{U}_w$ are generally very large, especially in the north part (X>2000m) where the standard deviations are larger than 0.4. However, the standard deviations of $\hat{H}_s$ are smaller than 0.15 and those of $\hat{T}_p$ less than 0.1. This implies that the mean wind speed has more prominent inhomogeneity than the significant wave height and peak period.

Regarding the inhomogeneity in terms of wind direction, the mean values and standard deviations of normalized wind direction $\hat{\theta}_{wi}$ across the fjord are shown in Fig. 13 under two threshold values of significant wave heights. In general, the mean values of $\hat{\theta}_{wi}$ vary within 10 degrees; nevertheless, the standard deviations of $\hat{\theta}_{wi}$ vary significantly and can reach about 90 degrees. This indicates that the wind direction across the fjord does not present a certain pattern as those of wave direction shown in Fig. 11. Similar as the mean wind speed, the wind directions in the south part has a relatively smaller variation than those in the north part.

4.2. Inhomogeneity in environmental parameters with waves from east

In this section, the inhomogeneity in environmental conditions with waves from east is analyzed. Two threshold values of significant wave heights, i.e., 0.3m and 0.6m, are also utilized here.

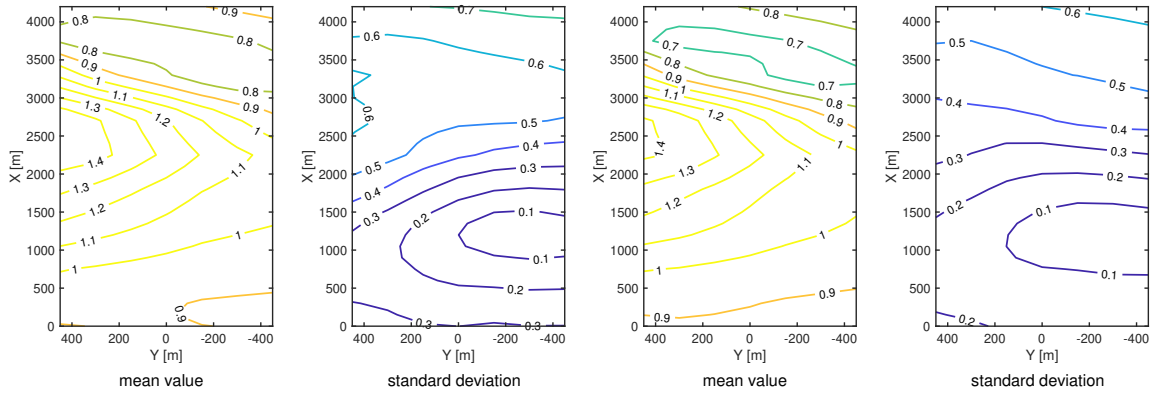

(a) $H_{s,thr}$ = 0.3m (b) $H_{s,thr}$ = 0.6m

Figure 12: contour maps of mean values and standard deviations of normalized mean wind speed $\hat{U}_w$ across the fjord. Only environmental conditions with waves from northwest and with a significant wave height at the reference point larger than the threshold value $H_{s,thr}$ are considered here.

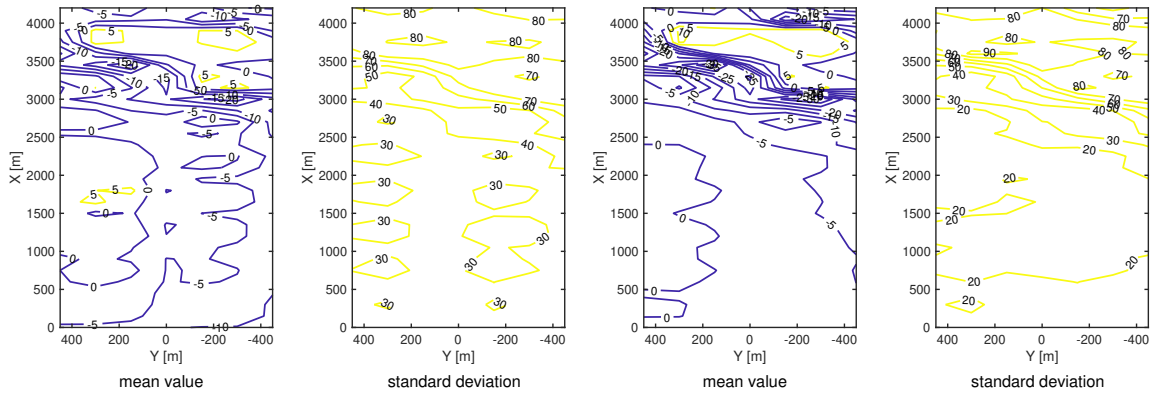

(a) $H_{s,thr}$ = 0.3m (b) $H_{s,thr}$ = 0.6m

Figure 13: contour maps of mean values and standard deviations of normalized wind direction $\hat{\theta}_{wi}$ across the fjord. Only environmental conditions with waves from northwest and with a significant wave height at the reference point larger than the threshold value $H_{s,thr}$ are considered here.

The results are presented in Figs. 14-18.

Fig. 14 presents the contour maps of mean values and standard deviations of normalized significant wave height $\hat{H}_s$ across the fjord where only waves coming from east are considered here. Under the threshold significant wave height of 0.3m, i.e. $H_{s,thr}$ = 0.3m, the mean values of the normalized significant wave height $\hat{H}_s$ are very close to 1 in the middle of the fjord (1000m<X<3800m). In the north part (X≥3800m) the mean values of $\hat{H}_s$ decrease rapidly while in the south part (X≤1000m), the mean values of $\hat{H}_s$ decrease relatively slowly from about 0.95 to 085. The standard deviations of $\hat{H}_s$ have a smallest value of about 0.02 in the middle of the fjord. Different from the mean values of $\hat{H}_s$, the standard deviation of $\hat{H}_s$ increase gradually from

the middle of the fjord to both ends. The largest value of the standard deviations of $\hat{H}_s$ are located in the north end, about 0.16. The mean values and standard deviations of $\hat{H}_s$ for the threshold significant wave height of 0.6m ($H_{s,thr}$ = 0.6m) have similar trends compared to those with the threshold significant wave height of 0.3m ($H_{s,thr}$ = 0.3m).

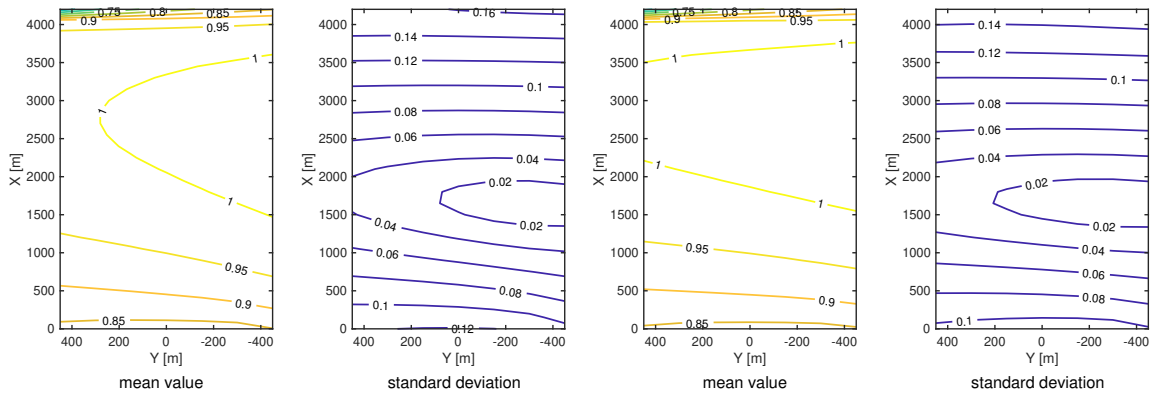

(a) $H_{s,thr}$ = 0.3m (b) $H_{s,thr}$ = 0.6m

Figure 14: contour maps of mean values and standard deviations of normalized significant wave height $\hat{H}_s$ across the fjord. Only environmental conditions with waves from east and with a significant wave height at the reference point larger than the threshold value $H_{s,thr}$ are considered here.

Fig. 15 shows the contour maps of mean values and standard deviations of normalized peak period $\hat{T}_p$ across the fjord where only waves coming from east are considered here. The mean values of $\hat{T}_p$ across the fjord are larger than 0.98, while the standard deviations of $\hat{T}_p$ is smaller than 0.03 in the middle and south part of the fjord (X≤3000m). In other part of the fjord, the standard deviations of $\hat{T}_p$ are slightly larger, but still less than 0.06. The standard deviations of $\hat{T}_p$ under the threshold significant wave height of 0.6m ($H_{s,thr}$ = 0.6m) is smaller than that under the threshold significant wave height of 0.3m ($H_{s,thr}$ = 0.3m). Therefore, the peak period across the fjord are almost identical for waves coming from east and with a significant wave height larger than 0.3m.

The wave directions across the fjord also present a pattern for wave coming from east and with a significant wave height larger than 0.3m, as shown in Fig. 16. Fig. 16 depicts the contour maps of mean values and standard deviations of normalized wave directions $\hat{\theta}_{wa}$ across the fjord. The mean values of $\hat{\theta}_{wa}$ increase gradually from about -15° in the south end to 25° in the north end. A relatively rapid increase is also found in the area close to the north end (X≥3800m). The standard deviations of $\hat{\theta}_{wa}$ increases gradually from the middle of the fjord to both ends and from east to west. The values of standard deviations of $\hat{\theta}_{wa}$ can reach about 6°, which is fairly large compared to the corresponding mean values of $\hat{\theta}_{wa}$. In addition, the standard deviation of $\hat{\theta}_{wa}$ under the threshold significant wave height of 0.6m are slightly smaller than those under the threshold significant wave

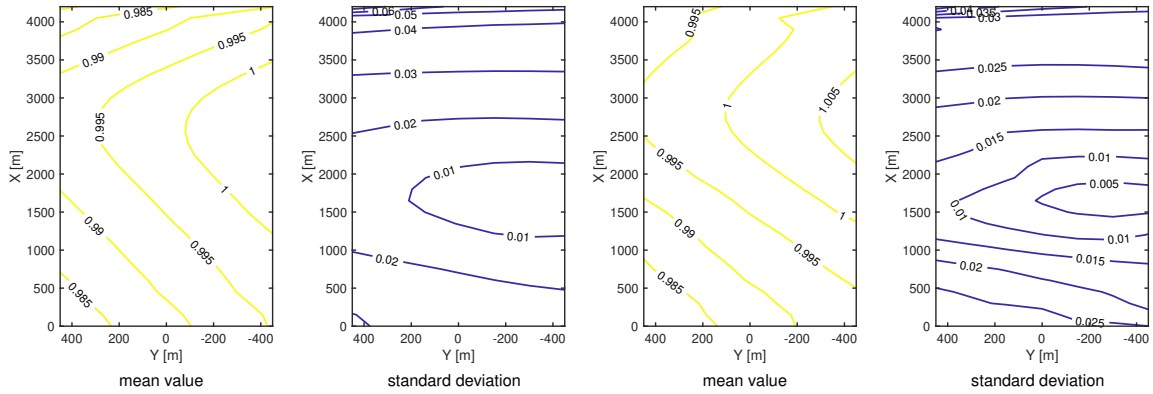

(a) $H_{s,thr}$ = 0.3m (b) $H_{s,thr}$ = 0.6m

Figure 15: contour maps of mean values and standard deviations of normalized peak period $\hat{T}_p$ across the fjord. Only environmental conditions with waves from east and with a significant wave height at the reference point larger than the threshold value $H_{s,thr}$ are considered here.

height of 0.3m.

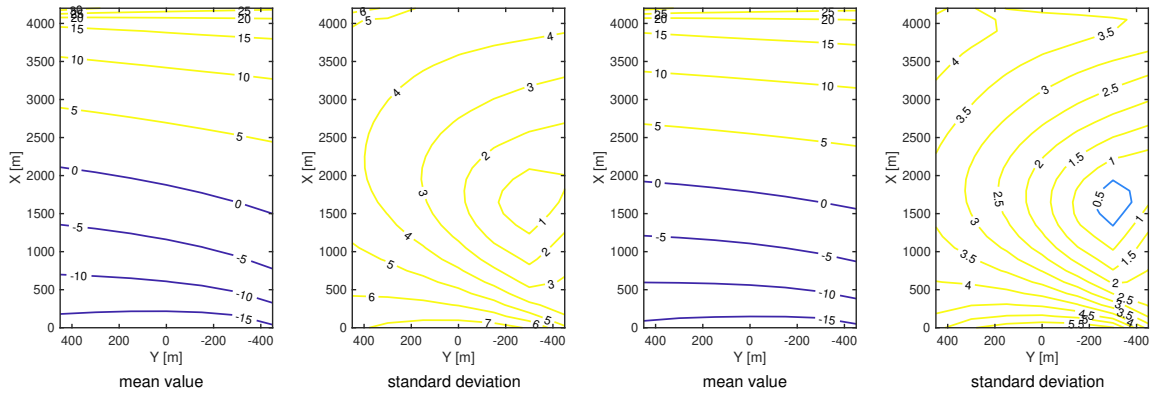

(a) $H_{s,thr}$ = 0.3m (b) $H_{s,thr}$ = 0.6m

Figure 16: contour maps of mean values and standard deviations of normalized wave direction $\hat{\theta}_{wa}$ across the fjord. Only environmental conditions with waves from east and with a significant wave height at the reference point larger than the threshold value $H_{s,thr}$ are considered here.

Figs. 14-16 present the contour maps of wave parameters ($\hat{H}_s$, $\hat{T}_p$, $\hat{\theta}_{wa}$) across the fjord for waves coming from east and with a significant wave height larger than 0.3m. Figs. 17-18 present the contour maps of wind parameters ($\hat{U}_w$, $\hat{\theta}_{wi}$). Compared to the contour maps of mean values and standard deviations of wave parameters, the contour maps of mean values and standard deviations of wind parameters present much greater variations across the fjord.

It can be found in Fig. 17 that under the threshold significant wave height of 0.3m ($H_{s,thr}$ = 0.3m), the mean values of normalized mean wind speed $\hat{U}_w$ varies from 0.7 to 1.2 across the fjord,

while the corresponding standard deviations of $\hat{U}_w$ can reach approximately 0.5. Significantly large variations of mean values and standard deviations of $\hat{U}_w$ are mainly observed in the north part of the fjord (X≥2000m). In the south part, these variations are relatively smaller compared to those in the north part. The standard deviations of $\hat{U}_w$ are approximately less than 0.25. Similar variations in mean values and standard deviations of $\hat{U}_w$ are also found under the threshold significant wave height of 0.6m ($H_{s,thr}$ = 0.6m). These variations are slightly smaller than those under the threshold significant wave height of 0.3m.

The mean values and standard deviations of normalized wind direction $\hat{\theta}_{wi}$ also demonstrate remarkable variations in the north part of the fjord (X≥2500m), as shown in Fig. 18. The mean values of $\hat{\theta}_{wi}$ vary from -30° to 10°, and the corresponding standard deviations of $\hat{\theta}_{wi}$ are larger than 30° and can even reach 100°. In the south part, the mean values of $\hat{\theta}_{wi}$ is about 10° while the standard deviation of $\hat{\theta}_{wi}$ are between 20° to 30°. The variations of mean values of standard deviations of $\hat{\theta}_{wi}$ in the south part are much smaller compared to those in the north part.

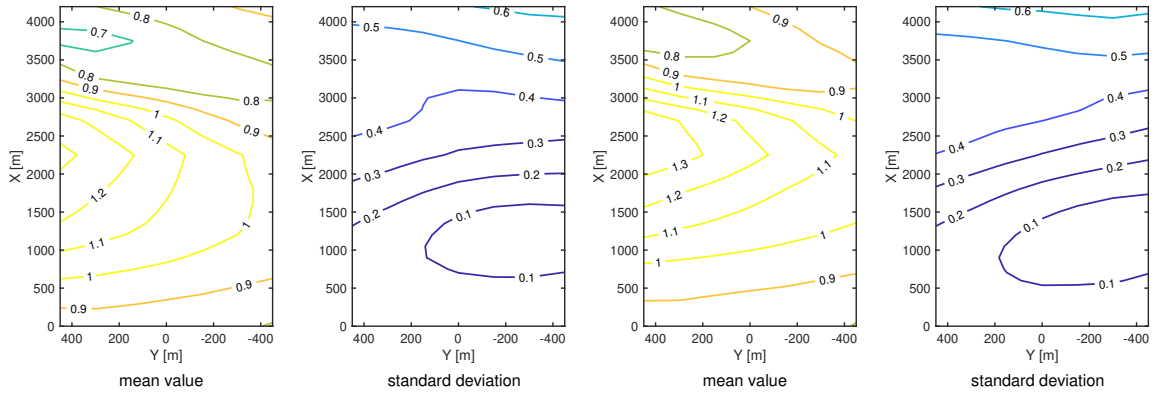

(a) $H_{s,thr}$ = 0.3m (b) $H_{s,thr}$ = 0.6m

Figure 17: contour maps of mean values and standard deviations of normalized mean wind speed $\hat{U}_w$ across the fjord. Only environmental conditions with waves from east and with a significant wave height at the reference point larger than the threshold value $H_{s,thr}$ are considered here.

5. Correlation of environmental parameters along a potential road route

This section addresses the correlation of environmental parameters based on the hindcast data. Correlation is usually described by the correlation coefficient, which is a statistical measure of linear relationship between two variables, A correlation coefficient of 1 means a perfect positive linear relationship between two variables.

From design of point view of floating bridges, the correlation of environmental parameters along the potential routes of floating brides are of great interest. For the considered fjord, several

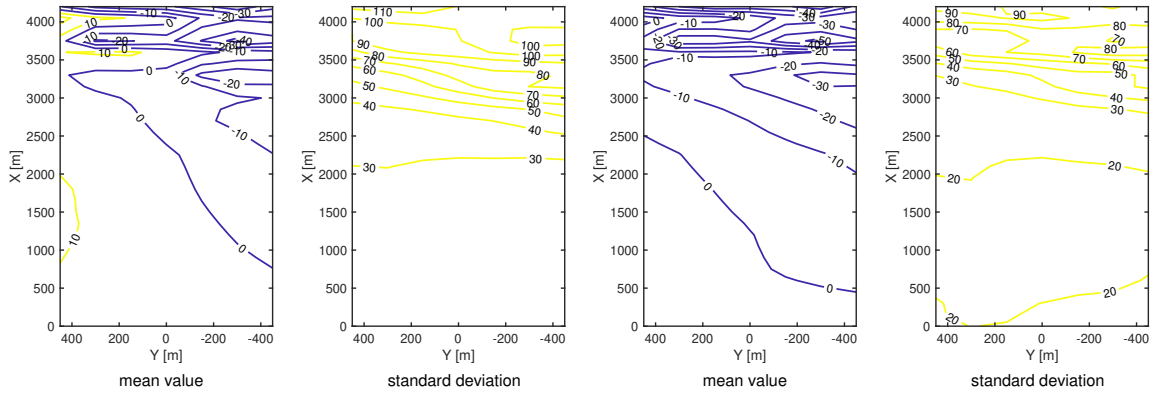

(a) $H_{s,thr}$ = 0.3m (b) $H_{s,thr}$ = 0.6m

Figure 18: contour maps of mean values and standard deviations of normalized wind direction $\hat{\theta}_{wi}$ across the fjord. Only environmental conditions with waves from east and with a significant wave height at the reference point larger than the threshold value $H_{s,thr}$ are considered here.

floating bridge concepts have been proposed and studied, included end-anchored curved floating bridges and side-anchored straight floating bridges. In this study, the potential route for side-anchored floating bridges are considered. This route is a straight line with Y=0 as shown in Figs. 1 and 7.

Environmental parameters at various grid points along the potential route considered are extracted from the hindcast data, including significant wave height, peak period, mean wave direction, mean wind speed and mean wind direction. The correlation of environmental parameters are studied by considering two dominant wave directions, i.e. from northwest and from east. The threshold significant wave height at the reference point is chosen to be 0.3m. The correlation matrix of wave and wind parameters among different grid points along the bridge route are thus estimated.

5.1. Correlation of environmental parameters with waves from northwest

The correlation matrix of environmental parameters along the bridge route is first analyzed for waves from northwest. Fig. 19 presents the correlation matrix of significant wave height, peak period and mean wave direction along the bridge route. In general, very high correlations (i.e. correlation coefficient greater than 0.95) are observed in these wave parameters among different pairs of points along the bridge route, except between grid points located in the south part and grid points in the north part. The peak period and mean wave direction at grid points in the south part (X≤3000m) have relatively small correlation with those in the north part. Regarding the peak period, only grid points located in the north with X≥4000m have a relatively small correlation with the other grid points.

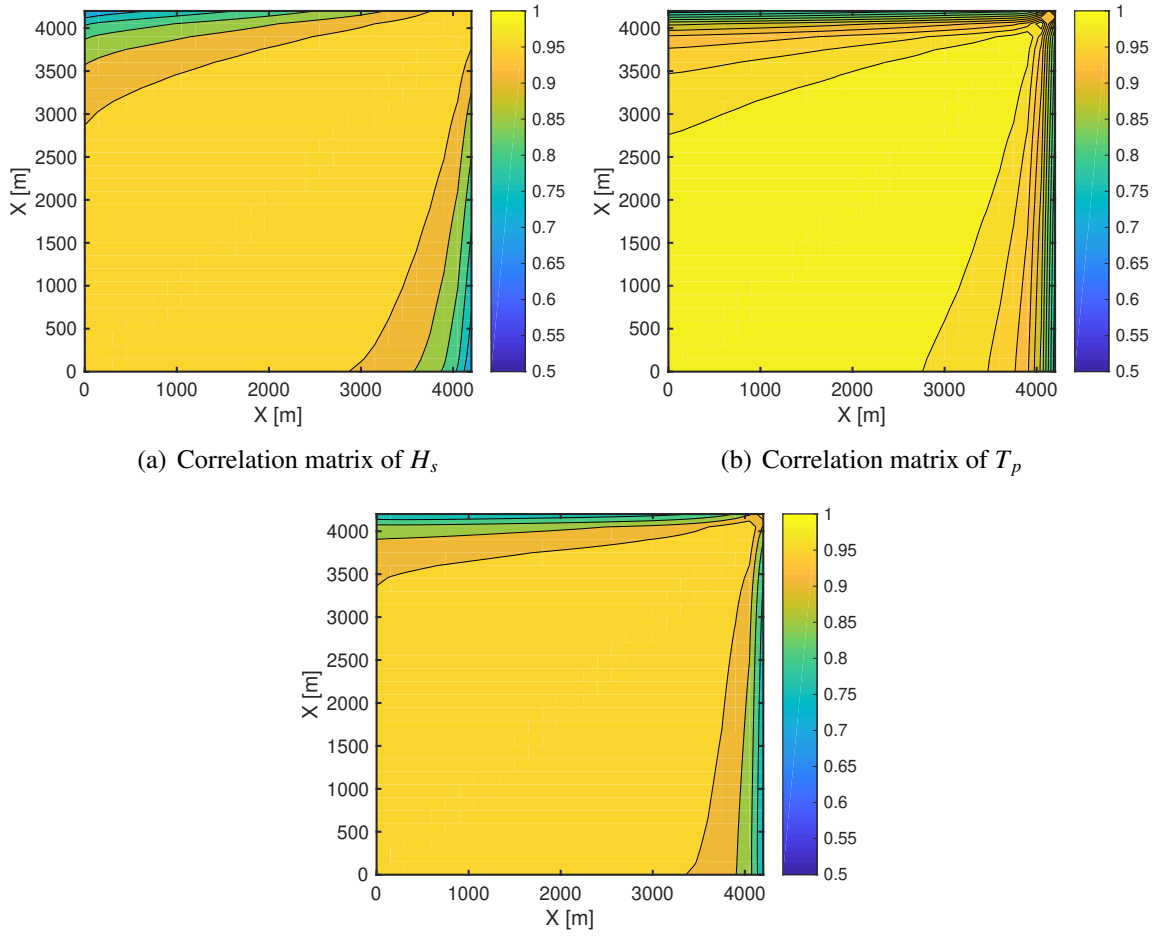

(a) Correlation matrix of H_s

(b) Correlation matrix of T_p

(c) Correlation matrix of θ_{wa}

Figure 19: Correlation matrix of wave parameters along the potential bridge route with waves from northwest and with a significant wave height larger than 0.3m. (a) significant wave height H_s, (b) peak period T_p, (c) mean wave direction θ_{wa}.

Fig. 20 shows the correlation matrix of mean wind speed and mean wind direction among different grid points along the bridge route. The correlation matrix of wind parameters differ greatly from those of wave parameters shown in Fig. 19. High correlations in mean wind speed are only observed between grid points that are close or are both located in the south part (X≤2500m). Very low correlation (with a correlation coefficient less than 0.1) are found between grid points located in the south part and those located in the north part. Regarding the mean wind direction, relatively high correlation coefficient is only observed between very close grid points while the correlation coefficient among most grid points are close to 0. This implies the mean wind direction along the bridge route has extremely weak correlation.

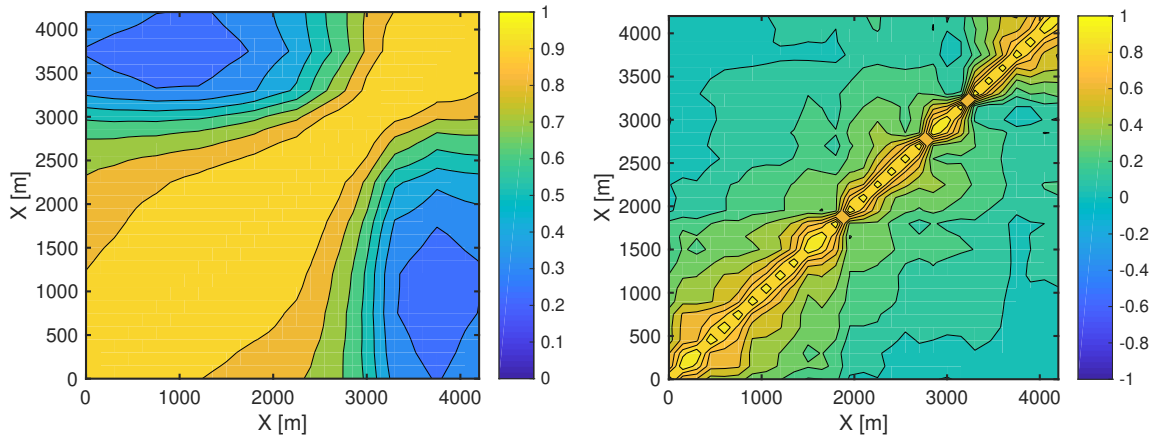

(a) Correlation matrix of U_w (b) Correlation matrix of θ_{wi}

Figure 20: Correlation matrix of wind parameters along the potential bridge route with waves from northwest and with a significant wave height larger than 0.3m. (a) mean wind speed U_w, (b) mean wind direction θ_{wi}.

5.2. Correlation of environmental parameters with waves from east

The correlation matrix of wave and wind parameters along the bridge route is also analyzed considering waves from east, as shown in Figs. 21 and 22. Fig. 21 shows the correlation matrix of significant wave height, peak period and mean wave direction along the bridge route considering waves from east. Two points along the bridge route with a distance less than about 1500m have a correlation coefficient larger than 0.95 in significant wave height, implying a very high correlation. The correlation decreases as the distance increases. The combination of point located at the south end and the other point at the north end gives a smallest correlation in significant wave height, with a correlation coefficient of about 0.72. Similar trends are also observed in the mean wave direction, but a high correlation in the south part requires a shorter distance between two points considered. The peak period has very high correlation among the whole bridge route, which is different from those shown Fig. 19(b) with waves from northwest.

The correlation matrix of mean wind speed and mean wind direction for waves from east are shown in Fig. 22. Relatively high correlations in mean wind speed are observed in the south part, which is similar as those shown in Fig. 20(a) with waves from northwest. Additionally, the correlation coefficients illustrated in Fig. 22(a) are overall larger than those shown in Fig. 20(a). Different from the correlation of mean wind direction for waves from north west shown in Fig. 20(b), the correlation of mean wind direction for waves from east are high in the south part.

6. Discussions

This study addresses the evaluation of inhomogeneity in wind and wave conditions in the Bjørnafjord based on 16-year hindcast data. The wave data (significant wave height, peak period

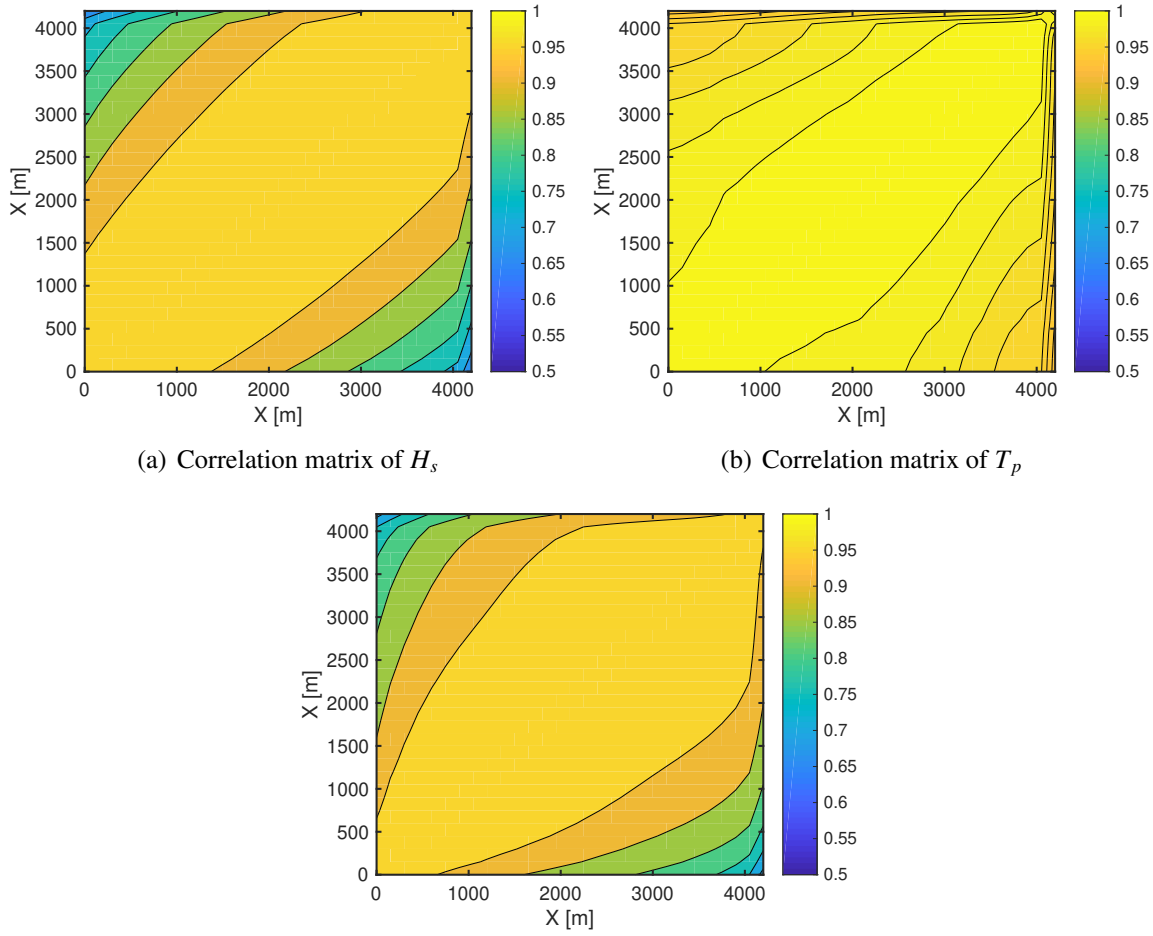

(a) Correlation matrix of H_s

(b) Correlation matrix of T_p

(c) Correlation matrix of θ_{wa}

Figure 21: Correlation matrix of wave parameters along the potential bridge route with waves from east and with a significant wave height larger than 0.3m. (a) significant wave height H_s, (b) peak period T_p, (c) mean wave direction θ_{wa}.

and mean wave direction) were simulated by using the SWAN model, which is developed based on the phase-averaged energy balance equation. Therefore, the SWAN model cannot provide the coherence spectra between any two points. Theoretically, coherence spectra can be calculated by using a phase-resolved wave model, such as potential flow based method and CFD-based method. The wave direction distribution is not addressed in this paper. However, it should be noted that although the SWAN model cannot provide the coherence spectra, it is much more efficient than the phase-resolved wave models and is thus suitable for large-scale long-term simulations. Besides, main features of the wave field at each point (e.g., significant wave height, peak period and mean wave direction) are captured by the SWAN model. These wave data are very important for ULS (Ultimate Limit State) design check of floating bridge.

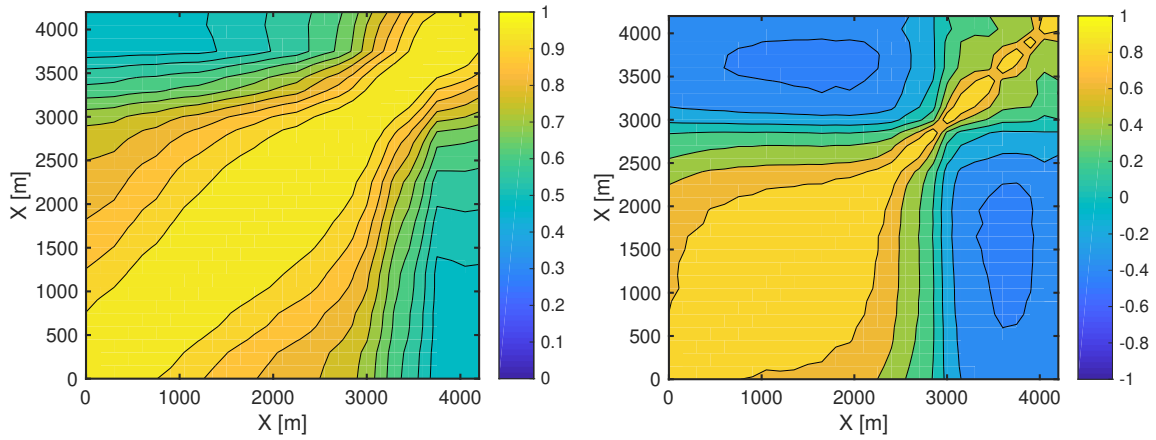

(a) Correlation matrix of U_w (b) Correlation matrix of θ_{wi}

Figure 22: Correlation matrix of wind parameters along the potential bridge route with waves from east and with a significant wave height larger than 0.3m. (a) mean wind speed U_w, (b) mean wind direction θ_{wi}.

The wind data (mean wind speed and direction) were simulated by using the WRF model. The WRF model is also a phase-averaged flow model that can provides the hourly-averaged wind speed at 10m height, while the wind shear, turbulence intensity are not accounted for yet. Besides, the coherence spectra of wind speed between two points in the space are not considered either. These wind data can be achieved by carrying out a 3D phase-resolved simulations (e.g. CFD), which is, unfortunately, extremely time-consuming and not suitable for engineering application. From point view of ULS design check of floating bridges, the mean wind speed plays an important role.

As a whole, though the present study does not provide a complete description of inhomogeneous wind and wave conditions in the fjord, it highlights the long-term spatial inhomogeneity in key wind and wave parameters, which are of great significance and useful for assessing the effects inhomogeneous environmental conditions on dynamic responses of floating bridges.

7. Conclusions

Long-term spatial inhomogeneity in wind and wave parameters for environmental conditions in a Norwegian fjord is evaluated in this study for design of floating bridges based on 16-year hindcast wind and wave data. The wave conditions are mainly characterized by significant wave height, peak period and mean wave direction, while the wind conditions are mainly described by mean wind speed and wind direction.

The wind and wave data are numerically simulated by using the WRF model and SWAN model, respectively. The accuracy of simulated wave data is first validated by comparison against field measurements. The time series of simulated H_s have an overall good agreement with the

measured H_s at all three wave buoy. Overall good consistency in the accuracy of simulation H_s is also observed. For waves with a significant wave height larger than 0.6m, model uncertainty of significant wave height at the three wave buoy are fairly close, with a mean value of approximately 0.77 and a CoV of about 0.23.

Inhomogeneity in wind and wave parameters within the potential area for deploying floating bridges are revealed by contour maps of normalized values. Two threshold value of significant wave height (i.e. 0.3m and 0.6m) and two dominant wave directions (i.e. waves from northwest and from east) are considered. When waves come from northwest, significant wave height and peak period are fairly close in the south part and decrease gradually towards the north end. Mean wave direction decreases from south end to north end. Mean wind speed has a relatively small variation in the south part and a great variation in the north part, so do the mean wind direction. Regarding waves from east, similar trends in the wave and wind parameters are observed but with slightly smaller variations compared to those with waves from northwest. Besides, standard deviations of the wind and wave parameters are generally small in the south part and become relatively large in the north part, especially for the wind parameters.

Correlation of wind and wave parameters along a potential bridge route is analyzed by considering waves with significant wave height greater than 0.3m and two dominant wave directions, i.e. waves from northwest and from east. It is found that distance between points greatly affects their associated correlations, especially when these two points are located in the south part and close to the north end, separately. For waves from northwest, wave parameters in the south part have high correlations; while for waves from east, distance between points less than 1500m can lead to high correlations in significant wave height and mean wave direction. Peak period is highly correlated when waves from east. Wind parameters are less correlated than the wave parameters. Mean wind speed is to some extent correlated in the south part.

To conclude, long-term spatial inhomogeneity in wind and wave parameters in the fjord is revealed by contour maps in this study. Together with the long-term joint distribution of wind and wave parameters, this study provides the environmental basis for evaluating the effects of inhomogeneous environmental conditions on extreme loads for ULS and cyclic loads for FLS, which are important for safety design of floating bridges. Based on present study, inhomogeneous environmental load effects of floating brides will be investigated in the future.

Acknowledgement

This work was supported by the Norwegian Public Roads Administration and in parts by the Research Council of Norway through the Centre for Ships and Ocean Structures (CeSOS) and Centre for Autonomous Marine Operations and Systems (AMOS), at the Department of Marine

Technology, NTNU, Trondheim, Norway. The support is gratefully acknowledged by the authors. The first author appreciates the support from the State Key Laboratory of Ocean Engineering (GKZD010075) and from the startup fund (WF220401010), Shanghai Jiao Tong University, Shanghai, China.

References

Booij, N., Ris, R.C., Holthuijsen, L.H., 1999. A third-generation wave model for coastal regions: 1. model description and validation. Journal of geophysical research: Oceans 104, 7649–7666.

Cheng, Z., Gao, Z., Moan, T., 2018a. Hydrodynamic load modeling and analysis of a floating bridge in homogeneous wave conditions. Marine Structures 59, 122–141.

Cheng, Z., Gao, Z., Moan, T., 2018b. Wave load effect analysis of a floating bridge in a fjord considering inhomogeneous wave conditions. Engineering Structures 163, 197–214.

Cheng, Z., Svangstu, E., Gao, Z., Moan, T., 2019a. Field measurements of inhomogeneous wave conditions in Bjørnafjorden. Journal of Waterway, Port, Coastal, and Ocean Engineering 145, 05018008.

Cheng, Z., Svangstu, E., Moan, T., Gao, Z., 2019b. Long-term joint distribution of environmental conditions in a norwegian fjord for design of floating bridges. Ocean Engineering 191, 106472.

Cheynet, E., Jakobsen, J.B., Snæbjörnsson, J., Mann, J., Courtney, M., Lea, G., Svardal, B., 2017. Measurements of surface-layer turbulence in a wide norwegian fjord using synchronized long-range doppler wind lidars. Remote Sensing 9, 977.

Dragani, W.C., Garavento, E., Simionato, C.G., Nuñez, M.N., Martín, P., Campos, M.I., 2008. Wave simulation in the outer rio de la plata estuary: evaluation of swan model. Journal of waterway, port, coastal, and ocean engineering 134, 299–305.

Engsig-Karup, A.P., Madsen, M.G., Glimberg, S.L., 2012. A massively parallel gpu-accelerated model for analysis of fully nonlinear free surface waves. International Journal for Numerical Methods in Fluids 70, 20–36.

Green, A.E., Naghdi, P.M., 1976. A derivation of equations for wave propagation in water of variable depth. Journal of Fluid Mechanics 78, 237–246.

Haver, S., 1980. Analysis of Uncertainties Related to the Stochastic Modelling of Ocean Waves. PhD thesis. Norwegian Institute of Technology.

Lothe, A., Musch, O., 2015. Bjørnafjorden submerged floating tube bridge: sea state simulations. Technical Report. Norconsult AS.

Madsen, P.A., Bingham, H., Liu, H., 2002. A new boussinesq method for fully nonlinear waves from shallow to deep water. Journal of Fluid Mechanics 462, 1–30.

Moan, T., Gao, Z., Ayala-Uraga, E., 2005. Uncertainty of wave-induced response of marine structures due to long-term variation of extratropical wave conditions. Marine Structures 18, 359–382.

Skamarock, W.C., Klemp, J.B., Dudhia, J., Gill, D.O., Barker, D.M., Huang, X.Y., Wang, W., Powers, J.G., 2008. A description of the advanced research WRF version 3. Technical Report. NCAR Tech. Note NCAR/TN-475+STR. National Center For Atmospheric Research, Boulder Colorado, USA.

Wang, W., Bihs, H., Kamath, A., Arntsen, Ø., 2017. Large scale CFD modelling of wave propagation in Sulafjord for the E39 project, in: Proceedings of the 9th National Conference on Computational Mechanics: MekIT 2017.